Comparison Analysis of Tendon-Driven Manipulators Based on Their Wrench Feasible Workspace

Nicolas J S Testard, Christine Chevallereau, Philippe Wenger

Comparison analysis of tendon-driven manipulators based on their wrench feasible workspace

Nicolas J.S. Testard, Christine Chevallereau, and Philippe Wenger

Nantes Université, Ecole Centrale de Nantes, CNRS, LS2N, 44000 Nantes, France
{Nicolas.Testard, Christine.Chevallereau, Philippe.Wenger, }@ls2n.fr

Abstract. This paper focuses on planar manipulators built upon stacking a series of tensegrity X-joints. The manipulators are actuated with four tendons, have different numbers of modules, with or without offsets. The objective of this work is to study the influence of offsets and number of modules on the size of the wrench-feasible workspace (WFW). The comparison analysis is conducted on the basis of equal manipulator height, width and mass and of equal maximal actuation forces. The spring constants pf the X-joints are determined so that the configuration at rest features a C-shape at a given end-effector pose with a minimal stiffness to ensure stability. We show that the more the number of modules, the larger the WFW, and that the offsets have little influence.

Keywords: tensegrity · wrench feasible workspace · tendon-driven

1 Introduction

Building modular manipulators brings many benefits. The number of modules should be decided upon considering several criteria, such as, the minimum number to accomplish the task, the possibility of having redundancy for a larger workspace, the cost or the weight. The bird neck can be a source of inspiration to build new light and efficient manipulators based on tensegrity modules arranged in series [1]. The tensegrity modules used in this paper have one degree of freedom (dof) and are operated by tendons as shown in Fig. 1, left. An antagonist actuation is chosen to allow modulation of the stiffness of the manipulator [2]. In this study, we are interested in planar manipulators made of several such modules arranged in series. An example with two modules and offsets is shown in Fig. 1, right.

A large amount of research work has been devoted to bio-inspired continuous-bodied manipulators [3]. Examples of manipulators inspired by animals are elephant-trunk arms [4,5,6], octopus' manipulators [7], snake-like manipulators [8], anguilliform manipulators [9].

The inspiration from musculoskeletal systems such as the bird neck or the human spine suggests that increasing the number of modules can increase performance. The object of the current study is to verify if this hypothesis is verified on the modular manipulators at hand.

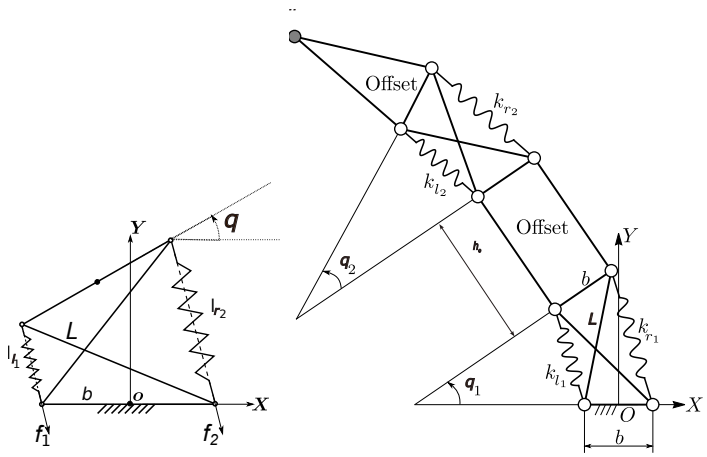

Fig. 1. X-joint tensegrity module (left) and manipulator made of two X-joints (right)

.

An important measure to quantify manipulator performance is the workspace size. Since manipulators under study are driven by tendons that can sustain only tensile forces, their workspace is further qualified by the condition of static equilibrium achievable with positive tendon forces. The rest of this paper is organized as follows. The manipulators studied are described in section 2. The calculation of the WFW is discussed in section 3. Section 4 compares different 4-tendon, fully actuated or under-actuated manipulators on the basis of their WFW. Last section concludes this paper.

2 Manipulators studied

The manipulators studied in this paper are planar manipulators with 4 tendons and n similar modules ($n \geq 3$) arranged in series. When $n > 3$, the manipulators are kinematically redundant since 3 dofs would be enough to control the end-effector motion in the plane. Moreover, $n > 3$ means that the manipulators are also under-actuated. Indeed, since the cables can only pull, one more cable than the number of modules should exist to control all the modules [10].

2.1 Tensegrity modules

We want to define a planar tensegrity manipulators inspired by the bird neck upon stacking several basic mechanisms or *modules*. These modules play the role of intervertebral joints. Each module consists of articulated bars and springs and are operated by cables. Springs and cables play the role of muscles and tendons. Tendon forces must be positive and are bounded by the actuators maximal torques. Since only planar motions are involved, the relative movement between two vertebrae is mainly a rotation. Both revolute joints and anti-parallelogram

joints (referred to as X-joint) can be used to produce planar motions between two vertebrae [11]. The former generate a pure rotation about a fixed point while the latter have a variable center of rotation. An important feature of the X-joint is its ability to increase stiffness under an increase in the antagonistic tendon forces, contrary to the revolute joint [12]. We thus decide to use X-joints (Fig. 1, left). The ratio between the length L of the crossed bar and the length b of the base or upper bar influences the kinetostatic performance of the X-joint but should also take into account the maximal and minimal elongation of the springs [13]. Different numbers of modules, with or without offsets will be considered in this work. Figure 1, right shows a manipulator built with two X-joints and offsets.

2.2 Stack of modules

The manipulators at hand are composed of a stack of modules. The stack can be build with or without offsets. Offsets can be viewed as the possibility to adjust the dimension of the vertebrae or, equivalently, the maximal reach of the manipulator, independently of the X-joints ratio L/b.

Let define the joint configuration of the manipulator by $\mathbf{q} = [q_1, q_2, ..., q_n]$, where n is the number of modules. Let $\mathbf{X} = [x_n, y_n, \gamma_n]$ define the pose of the end-effector (EE), i.e. the coordinates of the center of the upper bar of the last module n and its orientation angle. We have:

$$\begin{cases} x_n = -\sum_{i=1}^{n} \sin(\gamma_{i-1} + \frac{q_i}{2}) \sqrt{L^2 - b^2 \cos^2(\frac{q_i}{2})} - \sum_{i=1}^{n} \sin(\gamma_i) h_o \\ y_n = \sum_{i=1}^{n} \cos(\gamma_{i-1} + \frac{q_i}{2}) \sqrt{L^2 - b^2 \cos^2(\frac{q_i}{2})} - \sum_{i=1}^{n} \cos(\gamma_i) h_o \\ \gamma_n = \gamma_0 + \sum_{i=1}^{n} q_i \end{cases} \quad (1)$$

where h_o is the offset height (Fig. 1, right), γ_0 is the orientation angle of the base bar of the first module and $\gamma_i = \gamma_{i-1} + q_i$.

2.3 Tendon routing

For a planar manipulator, three dofs are sufficient to control its EE pose. We use n_f=4 tendons with remote motors on the base, regardless of the number of modules, in order to reduce inertia, complexity and costs. We also operate our manipulator with a long tendon connected to all the modules on the left side and 3 shorter tendons grouping together sub-groups of modules (see Fig. 2).

This choice results from a simplified implementation of the muscle organization of the bird neck [1,14]. We will also consider fully actuated manipulators, namely, manipulators with 3 modules actuated by a long tendon connecting the 3 modules on the left and 3 short tendons on the right. These short tendons actuate each of the modules independently, like in the prototype analyzed in [15].

Each tendon can be routed in different ways on each of the modules (Fig. 3):

- tendon j placed on the left or on the right of module i, along the spring (Fig. 3, left): when pulling this tendon, the associated motor modifies the module orientation so as to reduce the tendon length on this side;

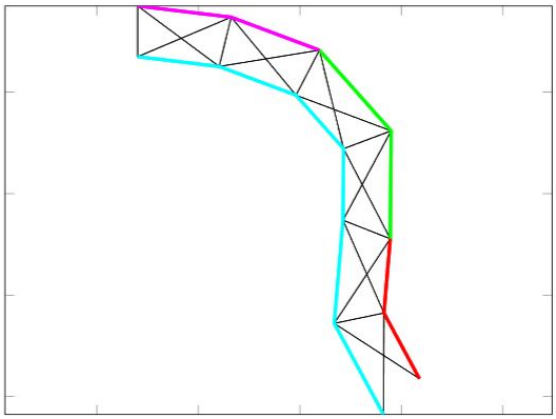

Fig. 2. Example of cable routing with 6 modules: one long cable on the left and three shorter cables on the right.

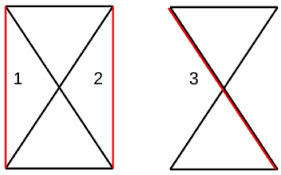

Fig. 3. Tendon routing situations.

- tendon j run along the bars of module i (Fig. 3, right): this routing allows reaching the modules located above module i while nullifying tendon impact on this module.

We define an actuation matrix $\mathbf{A}$ of size $(n \times n_f)$ as follows: each column j associated with tendon j describes how this tendon passes along module i. Each entry $A(i,j)$ can take on three possible values: 1 if the tendon passes on the left, 2 if the tendon passes on the right, 3 if the tendon j does not act on module i.

The unwounded length of tendon j is denoted by l_j.

The tendon length l_j can be expressed as follows [15]:

$$l_j = l_j^c + \sum_{i=1}^{n} l_j^{A(i,j)}(q_i) \tag{2}$$

where l_j^c is a constant value. $l_j^{A(i,j)}$ depends on the tendon routing:

$$\begin{cases} l_j^1 = \sqrt{L^2 - b^2\cos^2(\frac{q_i}{2})} + 2h\cos(\frac{q_i}{2}) - 2r\sin(\frac{q_i}{2}) \\ l_j^2 = \sqrt{L^2 - b^2\cos^2(\frac{q_i}{2})} + 2h\cos(\frac{q_i}{2}) + 2r\sin(\frac{q_i}{2}) \\ l_j^3 = 0 \end{cases} \tag{3}$$

3 Wrench-feasible workspace

3.1 Static model

The static model is of primary importance for the study of tensegrity manipulators. For a manipulator built with several modules in series, the static model allows determining its configuration as functions of the tendon forces. The potential energy U of the manipulator can be written as:

$$U = U_g + U_k + \sum_{i=1}^{4} F_j l_j, \tag{4}$$

where U_g (resp. U_k) is the contribution of gravity (resp. of all springs), l_j are the tendon lengths and F_j are the tendon forces. Each term $F_j l_j$ accounts for the potential energy associated with the work done by the cable forces. The equilibrium condition of the manipulator is:

$$\frac{\mathrm{d}U}{\mathrm{d}\mathbf{q}} = 0 \tag{5}$$

Let $\mathbf{G} = \frac{\mathrm{d}U_g}{\mathrm{d}\mathbf{q}} + \frac{\mathrm{d}U_k}{\mathrm{d}\mathbf{q}}$ and $\mathbf{Z}(\mathbf{q}) = -\frac{\mathrm{d}\mathbf{l}}{\mathrm{d}\mathbf{q}}$, where $\mathbf{l} = [l_1, l_2, l_3, l_4]^T$ and $\mathbf{F} = [F_1 ... F_4]^T$. The above equation can written as:

$$\mathbf{G}(\mathbf{q}) = \mathbf{Z}(\mathbf{q})\mathbf{F} \tag{6}$$

The associated linearized model writes:

$$\left(\frac{\mathrm{d}\mathbf{G}(\mathbf{q})}{\mathrm{d}\mathbf{q}} - \frac{\mathrm{d}\mathbf{Z}(\mathbf{q})\mathbf{F}}{\mathrm{d}\mathbf{q}}\right)\delta\mathbf{q} = \mathbf{Z}(\mathbf{q})\delta\mathbf{F} \tag{7}$$

An equilibrium is stable if its stiffness matrix is definite positive:

$$\mathbf{K} = \frac{\mathrm{d}^2 U}{\mathrm{d}\mathbf{q}^2} > 0 \tag{8}$$

3.2 WFW calculation

Tendons impose positive forces and these forces are bounded by the actuators. The set of poses that satisfy the abovementioned constraints and in which the robot can balance a bounded set of external wrenches is called the wrench-feasible workspace (WFW) [16]. In our case, the external wrenches are contributed by the springs and the gravity effects only. In the literature, the WFW is most often calculated for cable-driven parallel robots, see [16] and references herein. These methods cannot be adapted easily to serial tendon-driven manipulators. Continuation methods have been employed to compute the WFW of a 2-dof tensegrity manipulator [17]. The time taken for such computations has not been presented. A brute-force scanning technique has been followed in [13], where a 2-dimensional (D) scanning was performed in the joint space of a 2-DoF

manipulator to determine the WFW. The limitation of such a technique is that a high scanning resolution is required to obtain the boundary points with sufficient accuracy, which is untractable for manipulators with more than 3 modules. Interval analysis has been used to compute manipulator workspaces [18] or cable-driven parallel robots [16] with garanteed results but the high computational cost limits its practical implementation to manipulators with few dofs.

Joint space scanning A simple approach is to scan the joint space as proposed in [1]. The linearized model (7) is solved to determine a vector of forces $\mathbf{F}$ satisfying (7). When the number of tendons n_f is greater than the number of modules n, there exist infinitely many solutions and one can select the solution with minimal norm such that $0 < F_j < F_{max}$. This method cannot be used in our case for two major reasons. First, the computational cost increases exponentially with the number of modules and second, it does not work for under-actuated manipulators (i.e. when $n > n_f$). For those latter, indeed, the static model admits solutions only if $rank([\mathbf{G}(\mathbf{q}) \;\; \mathbf{Z}(\mathbf{q})]) = rank(\mathbf{Z}(\mathbf{q}))$.

Force space scanning Scanning the force space is more realistic since we have only 4 forces, whatever the number of modules. For each $\mathbf{F}$, it is then necessary to solve Eq. (6) to find the equilibrium configuration $\mathbf{q_e}$. We then calculate the EE coordinates via Eq. (1).

As observed in [2,13], several equilibrium solutions $\mathbf{q_e}$ can be obtained under two conditions: (i) the X-joints can reach a configuration close to their flat singularities and (ii) the gravity effects are dominant. In our case, the spring effects are very high as compared to gravity and the joint ranges are limited, so that there is only one feasible solution to Eq. (6). The equilibrium solution $\mathbf{q_e}$ is obtained iteratively, starting from the equilibrium configuration at rest. For a given set of input forces $\mathbf{F_e}$, we seek for the solution $\mathbf{q_e}$ that minimizes $||\mathbf{G}(\mathbf{q_e}) - \mathbf{Z}(\mathbf{q_e})\mathbf{F_e}||$, using a Newton-Raphson approach. Starting from a configuration $\mathbf{q_{ep}}$, this method consists in writing the linearized model (7) in the neighborhood of this configuration. We compute the variation that tends to nullify $||\mathbf{G}(\mathbf{q_e}) - \mathbf{Z}(\mathbf{q_e})\mathbf{F_e}||$. The joint solution is thus updated as follows:

$$\mathbf{q_e} = \mathbf{q_{ep}} - \left(\frac{\mathrm{d}\mathbf{G}(\mathbf{q_{ep}})}{\mathrm{d}\mathbf{q}} - \frac{\mathrm{d}\mathbf{Z}(\mathbf{q_{ep}})}{\mathrm{d}\mathbf{q}} \mathbf{F_e} \right)^{-1} (\mathbf{G}(\mathbf{q_{ep}}) - \mathbf{Z}(\mathbf{q_{ep}})\mathbf{F_e}) \tag{9}$$

The solution is updated until:

$$||\mathbf{G}(\mathbf{q_e}) - \mathbf{Z}(\mathbf{q_e})\mathbf{F_e}|| < \epsilon \tag{10}$$

where ϵ is a decision parameter, which we take here as $\epsilon = 1.e-6$. The matrix that needs to be inverted in (9) is in fact the stiffness matrix $\mathbf{K}$ defined in Eq. (8). Convergence is thus guaranteed whenever the equilibrium configurations are stable. On the other hand, the springs are selected such that the equilibrium configuration at rest is stable (see further). We thus expect that a stable equilibrium solution is always found. In fact, we have been able to verify that it is indeed

the case in all tested examples. Convergence speed depends on the starting configuration $\mathbf{q_{ep}}$, which must be close to $\mathbf{q_e}$. We start the force space scanning at $\mathbf{F} = \mathbf{0}$, namely, at the (stable) equilibrium configuration at rest. Convergence proves quite fast, after only 2 or 3 iterations in all tested examples. The WFW is then built in the 3D (x_n, y_n, γ_n) space upon calculating the EE pose associated with each equilibrium configuration.

The force and workspace sampling data used are as follows. The maximal forces are fixed to 140 N. We limit the number of tested forces to 20 for each tendon. Nature often relies on frugality. Therefore, bio-inspiration leads us to minimize energy. Accordingly, our objective is to move with minimum actuation forces. This goal can be achieved by trying to remain close to the equilibrium configuration at rest. Since we are interested to poses that can be reached with small forces, we choose a non-regular sampling to explore more values for low forces. The tested forces are $[0, 1, 2, 3, 5, 7, 9, 12, 16, 20, 25, 30, 35, 40, ...125, 130, 135, 140]$ for each tendon. To plot the WFW, we define a regular grid along the x_n, y_n and γ_n coordinates. The grid is built in a box defined by $\pm 1.1h$ along x_n and y_n and $\gamma_0 \pm nq_{max}$ along γ_n, where h is the manipulator height in its vertical straight configuration, q_{max} is the maximal bending angle of the X-joints and γ_0 is the orientation of the base bar of the first module. A WFW cell is declared reachable as soon as one pose of the EE belongs to it.

4 WFW comparative analysis

The goal of this section is to compare manipulators with different numbers of modules, with or without offsets. For more realistic comparisons, we impose similar features to all the manipulators studied:

- all modules in a given manipulator are identical with symmetric joint ranges $\pm q_{max}$;
- all manipulators have the same height h in their straight vertical configuration;
- for all manipulators, the sum of the rotation ranges of all their joints $\Delta q = 2nq_{max}$ is the same;
- all manipulators have the same width b;
- all manipulators have the same mass, assumed equally distributed in all the modules;
- all manipulators have the same EE pose in their rest configuration;
- stiffness in the rest configuration is greater than a given minimal value to ensure stability.

A first objective is to study the effect of offsets and module height (defined by L/b) on the WFW size, for completely actuated manipulators, i.e. with three modules. The bird neck includes a large number of vertebrae. However, it is not clear if manipulators with a large number of modules would be a right choice, as the actuation system of our manipulators is a highly simplified implementation of the complex muscle organization of the bird neck. A second objective is thus to study the effect of the number of modules on the WFW size.

4.1 Manipulator data

Manipulator compared For given module dimensions L and b, the module height in its zero orientation is $h_m = \sqrt{b^2 + L^2}$. We start with modules similar to those used in the prototype analyzed in [15]. Their geometric parameters are $b = 0.05$ m and $L = 0.1$ m. The corresponding module height is 0.0866 m. We fix the manipulator height of all manipulators to 6 times this module height: $h = 0.516m$. The joint range decreases with the number of modules in order to keep the same sum of joint ranges $\Delta q = 2nq_{max}$ (see above).

We consider 7 manipulators, described in table 1. Four of them have 3 modules with offset of values $h_o = 0$, $h_o = h_m$, $h_o = 2h_m$, and $h_o = 3h_m$, respectively. Besides, we take three offset-free manipulators with different numbers of modules, namely, 6, 9 and 12.

In all tested cases, the configuration at rest is defined as follows.The orientation angle of the manipulator base and the one of the EE bar are fixed to $\pi/4$ and $-\pi/4$, respectively, and the EE position is fixed at $x_m = 0$ and $y_m = 0.9h$. The choice of these data allows the manipulators to feature a C-shape equilibrium configuration at rest. Although the rest configuration of the bird neck features a S-shape [14], this shape is difficult to reach for manipulators with 3 modules only. In a C-shape configuration, the manipulator is not in a singularity and it can thus move more easily in all directions, like in a S-shape configuration. Finally, the sum of joint ranges is fixed to $\Delta q = 3pi$ and, to have a stable configuration, we impose a minimal stiffness at rest. This stiffness at rest can be obtained with suitable spring constants (see below).

Spring selection An essential element for the dimensioning of our manipulators is the choice of springs. The springs make it possible to define the equilibrium configuration at rest. The stiffer the springs, the higher forces are needed to move the manipulator and, for the same maximal forces, the more the WFW is reduced. On the other hand, the role of the springs is to ensure the stability of the manipulator. It is particularly important that the equilibrium configuration at rest be stable. This allows the manipulator to remain in this configuration under small perturbations and without any actuation. The springs are thus chosen on the basis of the following 2 requirements:

- impose a C-shape configuration at rest in the prescribed EE pose;
- ensure stability at rest. We impose a positive stiffness via the smallest eigenvalue of the stiffness matrix $\mathbf{K}$, which must be greater than a prescribed minimal value $K_m = 1$ Nm/rad.

We want to limit the spring stiffnesses, while satisfying the above constraints. The difference in stiffness between the 2 opposite springs in a module will modify the equilibrium configuration at rest while the average value of the springs will contribute to the X-joint stiffness.

For those manipulators with 3 modules, the configuration is fully defined by the EE pose. For the other manipulators, we first determine the equilibrium

configuration $\mathbf{q_e}$ which makes it possible to reach the desired EE position x_n^d, y_n^d, γ_n^d while minimizing the norm of the joint configuration vector :

$$\begin{aligned} \mathbf{q_e} &= min_q ||\mathbf{q}|| \\ & s.t. [x_n(\mathbf{q}), y_n(\mathbf{q}), \gamma_n(\mathbf{q})] = [x_n^d, y_n^d, \gamma_n^d] \end{aligned} \tag{11}$$

We then calculate the spring constants as follows:

$$\begin{aligned} [k_l \;\; k_r] &= min ||k_l + k_r|| \\ & s.t. \begin{cases} \mathbf{G}(\mathbf{q_e}) = \mathbf{0} \\ min(eig(\mathbf{K}(\mathbf{q_e}) \geq K_m \end{cases} \end{aligned} \tag{12}$$

The spring constants for the 7 manipulators compared are given in Table 1.

n	offset	q_{max}	Spring constants [N/m]
3	0	$\pi/2$	k_l=[1816 1339 874] k_r=[3860 3216 1512]
3	h_m	$\pi/2$	k_l=[1592 1454 593] k_r=[4346 3001 2278]
3	$2h_m$	$\pi/2$	k_l=[1283 1563 452] k_r=[4979 2821 3303]
3	$3h_m$	$\pi/2$	k_l=[1042 1710 369] k_r=[5843 2762 4835]
6	0	$\pi/4$	k_l=[2859 2780 2401 1825 1190 676] k_r=[5258 4692 3851 2832 1813 1027]
9	0	$\pi/6$	k_l=[3804 3826 3637 3268 2761 2171 1562 1003 593]
			k_r=[6608 6175 5579 4837 3987 3087 2207 1426 858]
12	0	$\pi/8$	k_l=[4708 4770 4679 4444 4085 3624 3090 2513 1929 1374 891 547]
			k_r=[7947 7586 7111 6526 5842 5080 4268 3440 2630 1879 1234 772]

Table 1. Robot data.

4.2 Example: a manipulators with 6 modules

In this section, we describe the case of a 6-X manipulator without offsets in order to provide some complementary information. Its data are given in Table 1, manipulator 5.

Figure 4 depicts the 3D WFW. Its shape looks like a twisted banana. This shows that the position and orientation coordinates are highly coupled. Moreover, the banana is rather flat, which shows that the EE orientation range is limited at every position. Therefore, the manipulator turns out to be more appropriate to positioning tasks. For now on, accordingly, the WFW will be analyzed in terms of point-reachable workspace, namely, as the set of points associated with at least one feasible EE orientation [19]. Figure 5 shows the resulting 2D WFW. The WFW was calculated for the minimal forces: the orientation was then fixed by the minimal forces at each point. Colors indicate the norm of the force vector.

4.3 Comparison results

Figure 6 shows the WFW of all compared manipulators. The WFW plots are arranged in a table with two columns and 4 rows. In each of the 4 rows, the

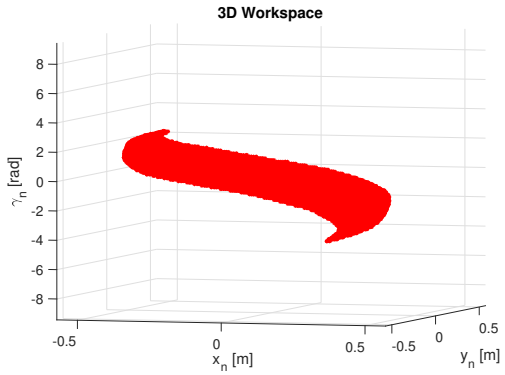

Fig. 4. Representation of the 3D WFW in (x_n, y_n, γ_n). The orientation of the effector varies significantly with the position of the effector but for a given pose, the orientation range is limited.

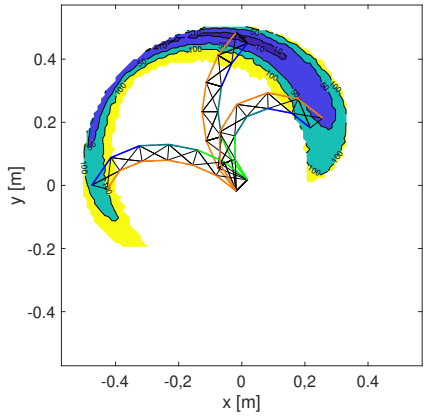

Fig. 5. WFW projected onto (x_n, y_n). The minimal forces have been considered at each point and colors indicate the norm of the force vector (dark blue: $||\mathbf{F}|| \leq 10$ N, blue: $10 < ||\mathbf{F}|| \leq 50$ N, green: 50 N $< ||\mathbf{F}|| \leq 100$ N, yellow:100 N $< ||\mathbf{F}||$). At the EE poses $[-0.45, 0]$ and $[0.24, 0.2]$, the manipulator is shown with its EE orientation corresponding to minimal forces.

manipulators have the same module ratio L/h. In the left columns, all the manipulators have 3 modules. The first one (resp. second, third, fourth) has no offsets (resp. offsets of height h_m, $2h_m$ and $3h_m$). The presence and height of offsets is difficult to analyze since the modules ratios L/b have different values for different offset numbers or heights. The second manipulator has clearly the largest WFW. This was expected since the module ratio of this manipulator satisfies the ideal ratio $L/b = 2$ [13]. Manipulators in the second row have no offsets. The first WFW of this row is the same as in the previous row for better visual comparison. Clearly, the more the number of modules, the larger the WFW. It is worth noting that it is still the case for the manipulators with 9 and 12 modules, although the module ratio L/b is smaller than the ideal value.

It is also interesting to compare each WFW of the first row with its neighbor in the second row (starting from the second row as the first row displays the same WFW), since their joint ratios are similar. The same conclusions as above can be drawn, namely, the WFW is larger when the number of modules is greater.

5 Conclusion

A family of planar manipulators built upon stacking a series of tensegrity X-joints has been analyzed in this paper. The manipulators are actuated with four tendons, regardless of the number of modules. The main goal of this work was to study the influence of offsets and number of modules on the WFW size. The comparison analysis was conducted on the basis of equal manipulator height, width and mass and of equal maximal actuation forces. The manipulators spring constants were determined so that the configuration at rest features a C-shape at a given EE pose with a minimal stiffness to ensure stability.

We have shown that the more the number of modules, the larger the WFW. Besides, the effect of offsets did not prove so significant. In fact, the module ratio turned out to be of more importance for manipulators with 3 modules. The WFW was calculated upon scanning the force space. Another possibility could be to scan the workspace. This will be the object of future work. Moreover, we will also study the influence of obstacles. Kinematically redundant and under-actuated manipulators should have a better ability to adapt to cluttered environments by shaping around obstacles.

References

1. B. Fasquelle, M. Furet, P. Khanna, D. Chablat, C. Chevallereau, and P. Wenger, "A bio-inspired 3-dof light-weight manipulator with tensegrity x-joints," in *2020 IEEE Int. Conf. on Robotics and Automation*, pp. 5054–5060, IEEE, 2020.
2. A. Van Riesen, M. Furet, C. Chevallereau, and P. Wenger, "Dynamic analysis and control of an antagonistically actuated tensegrity mechanism," in *ROMANSY 22–Robot Design, Dynamics and Control*, pp. 481–490, Springer, 2019.
3. D. Trivedi, C. Rahn, W. Kier, and Y. Parker, "Soft robotics: Biological inspiration, state of the art, future research," *Applied Bionics and Biomech.*, pp. 99–117, 2008.

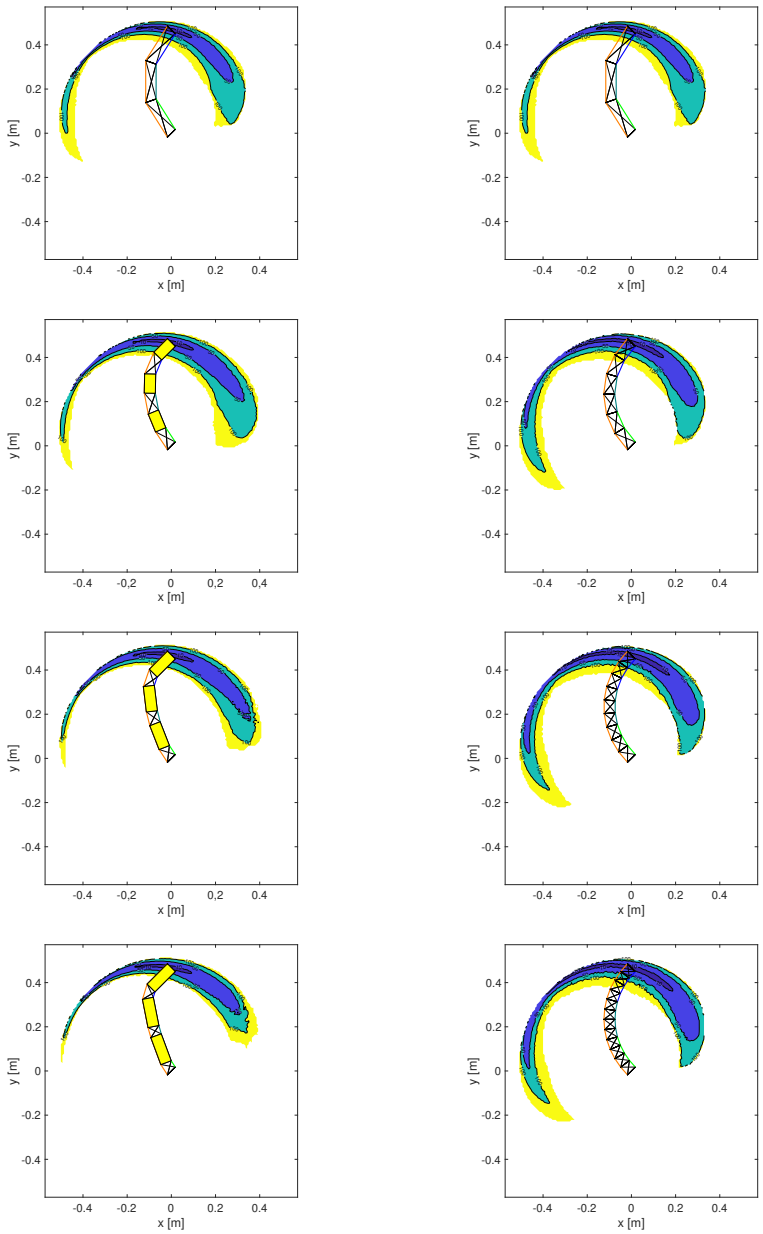

Fig. 6. Influence of the presence of offsets (first column) and of the number of modules (second column) on the WFW shape and size. The same WFW has been reproduced in the first row. The presence of offsets tends to reduce the WFW size, while a greater number of modules tends to increase the WFW size.

4. M. Hannan and I. Walker, "Analysis and initial experiments for a novel elephant's trunk robot," in *Proceedings. 2000 IEEE/RSJ Int. Conf. on Intelligent Robots and Systems*, vol. 1, pp. 330–337 vol.1, 2000.
5. Q. Guan, J. Sun, Y. Liu, N. M. Wereley, and J. Leng, "Novel bending and helical extensile/contractile pneumatic artificial muscles inspired by elephant trunk," *Soft Robotics*, vol. 7, no. 5, pp. 597–614, 2020. PMID: 32130078.
6. Y. Liu, Z. Ge, S. Yang, I. D. Walker, and Z. Ju, "Elephant's Trunk Robot: An Extremely Versatile Under-Actuated Continuum Robot Driven by a Single Motor," *Journal of Mechanisms and Robotics*, vol. 11, 07 2019. 051008.
7. C. Laschi, M. Cianchetti, B. Mazzolai, L. Margheri, M. Follador, and P. Dario, "Soft robot arm inspired by the octopus," *Advanced Robotics*, vol. 26, no. 7, pp. 709–727, 2012.
8. R. Buckingham, "Snake arm robots," *Industrial Robot*, vol. 29, no. 3, pp. 242–245, 2002.
9. M. Porez, F. Boyer, and A. J. Ijspeert, "Improved lighthill fish swimming model for bio-inspired robots: Modeling, computational aspects and experimental comparisons," *The International Journal of Robotics Research*, vol. 33, no. 10, pp. 1322–1341, 2014.
10. M. Carricato and J.-P. Merlet, "Stability analysis of underconstrained cable-driven parallel robots," *IEEE Transactions on Robotics*, vol. 29, no. 1, pp. 288–296, 2012.
11. M. Furet, A. Abourachid, C. Bohmer, V. Chummunb, C. Chevallereau, R. Cornette, X. D. L. Bernardie, and P. Wenger, "Estimating motion between avian vertebrae by contact modeling of joint surfaces," *Computer Methods in Biomechanics and Biomedical Engineering*, 2021.
12. V. Muralidharan and P. Wenger, "Optimal design and comparative study of two antagonistically actuated tensegrity joints," *Mechanisms and Machine Theory*, vol. 159, p. 104249, 2021.
13. M. Furet and P. Wenger, "Kinetostatic analysis and actuation strategy of a planar tensegrity 2-x manipulator," *ASME J. of Mechanisms and Robotics*, vol. 11, no. 6, p. 060904, 2019.
14. L. Terray, O. Plateau, A. Abourachid, C. Böhmer, A. Delapré, X. la Bernardie, and R. Cornette, "Modularity of the neck in birds (aves)," *Evolutionary Biology*, 2020.
15. B. Fasquelle, P. Khanna, C. Chevallereau, D. Chablat, D. Creusot, S. Jolivet, P. Lemoine, and P. Wenger, "Identification and control of a 3-x cable-driven manipulator inspired from the bird neck," *ASME J. of Mechanisms and Robotics*, pp. 1–25, 2021.
16. M. Gouttefarde, D. Daney, and J.-P. Merlet, "Interval-analysis-based determination of the wrench-feasible workspace of parallel cable-driven robots," *IEEE Transactions on Robotics*, vol. 27, no. 1, pp. 1–13, 2011.
17. Q. Boehler, I. Charpentier, M. Vedrines, and P. Renaud, "Definition and computation of tensegrity mechanism workspace," *Journal of Mechanisms and Robotics*, vol. 7, 2015.
18. D. Chablat, P. Wenger, F. Majou, and J. P. Merlet, "An interval analysis based study for the design and the comparison of three-degrees-of-freedom parallel kinematic machines," *The International Journal of Robotics Research*, vol. 23, no. 6, pp. 615–624, 2004.
19. R. Vijaykumar, K. Waldron, and M. Tsai, "Geometric optimization of serial chain manipulator structures for working volume and dexterity," *The International Journal of Robotics Research*, vol. 5, no. 2, pp. 91–103, 1986.